Optics Letters

Generation of vortex rosette via donut-shaped beams in optical valves

M. G. Clerc,[1] M. Diaz-Zuniga,[1,*] M. Kowalczyk,[2] and P. Smyrnelis[3]

[1]Departamento de Física and Millennium Institute for Research in Optics, FCFM, Universidad de Chile, Casilla 487-3, Santiago, Chile
[2]Departamento de Ingeniería Matemática and Centro de Modelamiento Matemático (UMI 2807 CNRS), Universidad de Chile, Casilla 170, Correo 3, Santiago, Chile
[3]Department of Mathematics, University of Athens, 11584 Athens, Greece
*manudiaz@ug.uchile.cl

Received 17 November 2025; revised 15 January 2026; accepted 16 January 2026; posted 20 January 2026; published 11 February 2026

Optical vortices have attracted significant interest due to their distinctive topological properties and wide-ranging applications, including free-space communication, quantum information, image analysis, and micromanipulation. Vortex formation can arise from the interaction of light with structured or anisotropic media, including chiral systems. Among the most effective platforms for generating optical vortex beams are optical valves and liquid crystal cells, which leverage molecular self-organization to produce complex light fields. We show, both experimentally and theoretically, that illuminating an optical valve with a donut-shaped beam generates a vortex rosette, consisting of a low-amplitude central vortex surrounded by a ring of interacting vortex–antivortex pairs. This structure imparts a nontrivial topological charge to the transmitted light, endowing it with novel characteristics akin to those of a q-plate. To elucidate the origin of these vortex rosettes, we derive an amplitude equation from first principles, offering insight into the underlying mechanisms driving their emergence.

https://doi.org/10.1364/OL.584445

Since the dawn of time, humanity has been intrigued by the behavior of light and its understanding. The advent of coherent light sources, lasers, and the generation of monochromatic, coherent, and directional beams has enabled a more profound and comprehensive understanding of light and its interaction with matter. The creation of light beams carrying orbital angular momentum (OAM) has been highly relevant in applying new functionalities of light [1], such as communications [2,3], astronomical [4] and microscopic image processing [5,6], quantum computing [6,7], orbital angular momentum lasers [8], and manipulating micrometric particles [9–11]. It has also opened fundamental questions about creating this beam type and its associated topological properties [12]. Various methods have been proposed for optical vortex generation, including spiral phase plates [13], diffractive elements [14,15], liquid crystal (LC) cells with radial director orientation, q-plates [16], LC droplets [17], and LC cells with umbilical defects [18] induced by magnetic fields and oscillatory electric fields [19,20]. Additionally, liquid crystal light valves [21–23] have been explored for this purpose. In most of these devices, a Gaussian beam is used as excitation or illumination light, which induces a unique angular orbital momentum in the light by transferring angular momentum.

Liquid crystal light valves (LCLVs) illuminated by a Gaussian beam induce an umbilical defect in the liquid crystal layer within the central illuminated region [23]. Near and below the orientation transition, the light forcing sustains a broad vortex-type defect in the liquid crystal layer, known as Rayleigh matter vortex [24,25]. Note that this topological structure closely resembles a Laguerre–Gaussian mode of a paraxial laser beam with topological charge $l = +1$. By modifying the illumination geometry, new classes of optical topological structures can be generated, opening pathways toward innovative applications of vortex beams.

The aim of this Letter is to show that illuminating a liquid crystal light valve with a donut-shaped beam induces *optical vortex rosette* (VROS) (see Fig. 1). These configurations arise from stable configurations of matter vortices on the illuminated region of the LCLV. These configurations consist of a central Rayleigh vortex surrounded by pairs of opposite vortices in equilibrium. These VROS increase the number of generated optical vortices, acting as a novel q-plate element. We experimentally demonstrate different VROS based on an optically driven LCLV with a transmission configuration and homeotropic anchoring. Figure 1 shows different configurations of induced vortices in matter. The total topological charge of the liquid crystal coupled vortices is one. To account for the VROS, near the reorientation instability of the liquid crystal, the system is described by the real Ginzburg–Landau equation with topological forcing [23]. Numerical simulations of the amplitude equation find excellent agreement with experimental observations.

The experimental setup for VROS generation is illustrated in Fig. 1(b), which consists of a liquid crystal light valve illuminated with a donut-shaped intensity profile. This intensity profile I_0 is achieved by applying a donut-shaped mask $\propto (r/\omega)^2 e^{-r^2/\omega^2}$, closely resembling the transverse structure of a Laguerre-Gauss beam, thanks to the use of a spatial light modulator (SLM). This beam is equivalent to an OAM-carrying beam profile. For the intensity profile, a diode-pumped solid-state

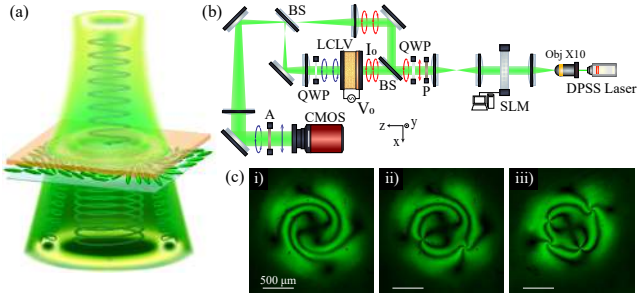

Fig. 1. Experimental setup for vortex rosette (VROS) in Liquid Crystal Light Valve (LCLV). (a) Schematic illustration of VROS induction. The upper green beam accounts for the incident light beam with a donut-shaped intensity profile without topological charge. (b) Schematic representation of experimental setup, where DPSS is a diode-pumped solid-state laser, L and M account for the lenses and mirrors considered, SLM is a spatial light modulator, P and A are the cross-polarizers, V_0 is the driven voltage, I_0 is the light intensity applied to LCLV, Obj stands for a microscope objective with a magnification of ×10, and CMOS is a complementary metal-oxide-semiconductor camera. The setup incorporates a Mach–Zehnder modified interferometer for circularly polarized light, where QWP are quarter-waveplates at $\pm 45°$ to linear into circular polarization, and vice versa. (c) Snapshots of experimental VROS at $V_0 = 18$ Vrms at 200 Hz, and $I_0 = 8$ mW/cm^2. VROS of (c(i)) single, (c(ii)) triad, and (c(iii)) quintet charges.

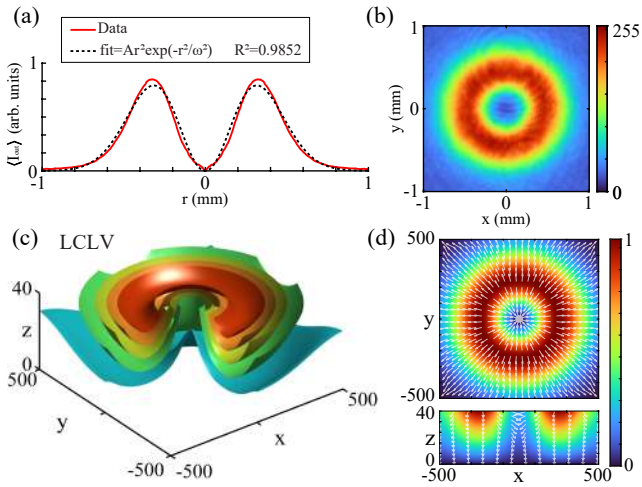

Fig. 2. Donut-shaped intensity profile effects on LCLV: (a) shows the experimental radial average intensity profile of the light beam induced in the LCLV. The red curve shows the average intensity profile, and the black dashed curve shows the experimental fit, $A_0 r^2 \exp(-r^2/\omega_0^2)$, with $A_0 = 25.41$ mm^{-2}, and $\omega_0 = 0.3159$ mm. (b) The experimental intensity profile for $I_0 = 8.02$ mW/cm^2. (c) The numerical solution of the equipotential surfaces of the Laplace equation in an anisotropic medium under the boundary conditions: $\Phi(x, y, z = 0) = 0$, $\Phi(x, y, z = 40) = (r/\omega)^2 \exp(-r^2/\omega^2) + 0.1$, with $\omega = 125$. (d.i) Transverse and (d.ii) longitudinal cross-section of the electric potential solution to the Laplace equation. The white arrows represent the normalized electric field associated with the potential.

laser with wavelength $\lambda_0 = 532$ nm, and TEM 00 light mode is employed. The beam is expanded by a microscope objective with a magnification of ×10, to control the beam shape with a spatial light modulator (SLM, LC 2012 Spatial Light Modulator Holoeye, transmission). This SLM is based on a twisted nematic liquid crystal display, which generates a simple phase modulation and a coupled polarization effect, resulting in amplitude modulation. The LCLV is situated between two crossed linear polarizers, enabling the observation of the polarization reorientation caused by the matter vortex. The vortex induction is monitored by a complementary metal-oxide-semiconductor (CMOS) camera.

To study the light–matter interaction, we implemented a crossed circular polarizer configuration by adding two quarter-wave plates to the setup: the first oriented at 45° to the input polarizer and the second with its fast axis perpendicular to the first. A modified Mach–Zehnder interferometer with a slight beam tilt produces a vertical interference fringe pattern.

The LCLV (provided by HOASYS) is composed of a nematic liquid crystal thin film (MLC 6608 Merck, elastic constants $K_1 = 16.7$ pN, $K_2 = 7.3$ pN, $K_3 = 18.1$ pN) deposited between two parallel glass plates, with a thickness of $d = 15$ μm. Two transparent conductive indium tin oxide (ITO) films and a transparent photoconductive slab of $Bi_{12}SiO_{20}$ (BSO) are included in the plates. The photoconductive slab has dimensions of 25×25 mm^2 and a thickness of 1 mm. The internal surfaces present homeotropic anchoring for the liquid crystal molecules, so that the nematic director is orthogonal to the confinement walls. The liquid crystal has a negative dielectric anisotropy $\epsilon_a = \epsilon_\parallel - \epsilon_\perp = 3.6\epsilon_o - 7.8\epsilon_o = -4.2\ \epsilon_o$, where $\epsilon_\parallel$ and $\epsilon_\perp$ are the dielectric susceptibilities for the parallel and orthogonal electric fields, respectively. By applying a perpendicular external electric field $\mathbf{E} = -V_0/d\ \hat{\mathbf{z}}$ in the LCLV, the competition between the elastic restitution forces and the external electric torque establishes a critical threshold for the electric field that induces a molecular reorientation, called Fréedericksz transition [FT1933], where vortex defects are generated in the liquid crystal system [23]. Notice an oscillating voltage V_0 Vrms is applied to the LCLV through the ITO films at a frequency $f = 200$ Hz. Due to the light–matter interaction, these liquid crystal matter vortices generate optical vortices in a light beam [21].

The photosensitive wall of the LCLV (BSO slab) generates charge movements when illuminated, inducing a localized, non-homogeneous voltage that is proportional to the light intensity at low values. Namely, the applied voltage to the liquid crystal layer takes the form $V = \Gamma V_0 + \alpha I_0$, $0 < \Gamma < 1$ is a transfer factor that depends on the electrical impedances of the photoconductor and liquid crystals layer, and α is a phenomenological dimensional parameter that describes the linear response of the photoconductor ($\alpha \sim 4$).

When the valve is illuminated with a donut-shaped light beam (see Fig. 2(b)), an extra voltage is induced of the form, $V_I = \alpha I(r) = \alpha A r^2 e^{-r^2/2\omega^2}$ where $r = \sqrt{x^2 + y^2}$ is the radial transversal coordinate. Figure 2(a) shows a comparison with the previous voltage V_I and the experimentally observed light profile, demonstrating a good agreement. To shed light on the voltage inside $\Phi(x, y, z)$, the liquid crystal cell, we solve the Laplace equation with appropriate boundary conditions. Figure 2 shows the obtained voltage. From this chart, one can infer that the Φ voltage has a semi-donut shape with different layers.

The inferred electric field $\mathbf{E} = -\nabla\Phi$ is shown in Fig. 2(d), where a vortex in the electric field is observed at the center of the illuminated ring region. Note that the electric field is vertical in the ring. At the center of the illuminated ring, a

small-amplitude matter vortex is sustained by topological forcing (Rayleigh vortex) surrounded by a ring that appears on the liquid crystal sample [see Fig. 1(c(i))]. Unexpectedly, when the intensity of the donut-shaped beam I_0 approaches 8 mW/cm^2, the region associated with the vertical electric field becomes unstable. This instability leads to the spontaneous formation of coupled matter vortex–antivortex pairs, which interact both with each other and with the central vortex, giving rise to stable VROS configurations. Depending on the generation protocol, three configurations are observed. The single VROS, obtained by gradually increasing the beam waist to $\omega_0 = 0.315$ mm. A VROS composed of three charges formed at $V_0 = 18$ Vrms by switching on the beam, where a vortex–antivortex pair nucleates at antipodal ring positions, as a consequence of their interaction [Fig. 1(c(ii))]. A similar vortex structure has been reported for liquid crystals under the effect of a homogeneous electric field and a magnetic field of a ring magnet [20]. Also, a higher-order state, including a stable VROS with five charges, was obtained by increasing the voltage from zero to $V_0 = 18$ Vrms [Fig. 1(c(vi))]. Videos illustrating the formation and stability of these VROS are provided in Visualization 1 [26].

In short, liquid crystal light valves illuminated with donut-shaped light induce different VROS.

To analyze the optical implications, let us now consider a circularly polarized incident plane wave $\mathbf{E}_{in} = \sqrt{I_0(\mathbf{r}_\perp)}\hat{\mathbf{e}}_\sigma e^{i(kz-\omega t)}$, where $\hat{\mathbf{e}}_\sigma = (1, i\sigma)$ is the circular polarization vector in a fixed reference frame, and $\sigma = \pm 1$ is the helicity. LCLV is a liquid crystal cell with homotropic anchoring, which alters the polarization of light by means of the operator [27–30]:

$$W(\phi,\theta) = e^{-i\Phi_{dyn}} R(\phi) \begin{pmatrix} e^{-i\frac{\Delta_-}{2}} & 0 \\ 0 & e^{i\frac{\Delta_-}{2}} \end{pmatrix} R(-\phi), \quad \textbf{(1)}$$

where ϕ, θ are the azimuthal and vertical angles, respectively, $R(\phi)$ is the rotation matrix, $\Delta_\pm = (2\pi n_o d/\lambda)\int_0^1 \left(\sqrt{\cos^2\theta_{(z)} + (n_o/n_e)^2 \sin^2\theta_{(z)}} \pm 1\right) dz$ is the phase retard induced by the birefringence media, and $\Phi_{dyn} = \Delta_+/2$, is the global dynamical phase. When a circularly polarized light beam is incident, the resulting output beam, after filtering the initial helicity through cross polarization is $\mathbf{E}_{out} = \sqrt{I_0(\mathbf{r}_\perp)}\sin(\Delta_-/2) e^{-i\Phi_{dyn}} e^{-i\frac{\pi}{2}} e^{i2\sigma\phi} \hat{\mathbf{e}}_{-\sigma} e^{i(kz-\omega t)}$. Notice the angle ϕ induces a Pancharatnam-Berry geometric phase, $\Phi_B = 2\sigma\phi$ [31,32]. When molecules form a matter vortex texture, the system acts as a q-plate element. In the case of VROS, it allows us to induce multiple vortices in a donut-shaped light beam. By fringe interferometry, using the Hilbert transform method to transform the interference pattern into a complex field, we can estimate the geometric phase induced on the light. Figure 3 shows the experimental estimations.

The behavior of liquid crystals is characterized by the direction vector $\mathbf{n}$, which represents the average orientation of the molecules. The evolution of the director is characterized by the minimization of the Frank-Oseen free energy, in which is included the effect of electrical energy and the constant norm constraint of the director $|\mathbf{n}| = 1$ [27–29]. Close to reorientational instability, by the ansatz $\mathbf{n} = \left[X\sin(\pi z/d), Y\sin(\pi z/d), 1-\left(X^2+Y^2\right)\sin^2(\pi z/d)/2\right] + \mathbf{W}(X,Y)$, where X and Y are scalar fields that represent the projection of the director onto the horizontal plane and $\mathbf{W}$ is a small nonlinear correction vector field.

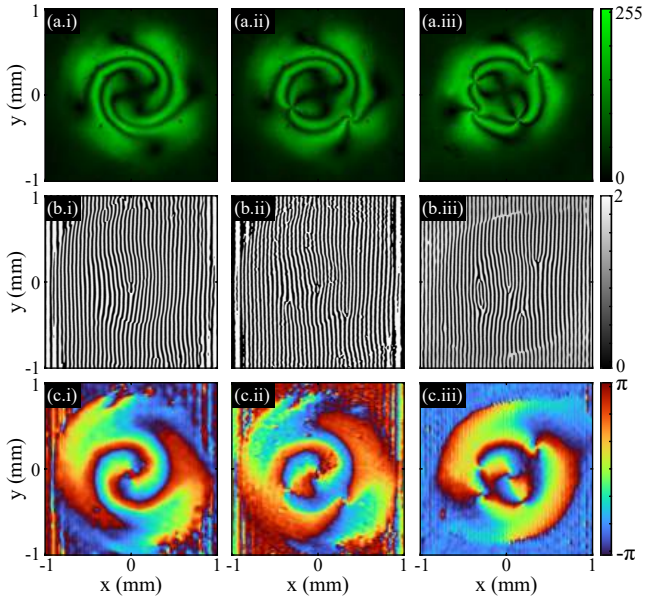

Fig. 3. Experimental results of optical vortex induction by liquid crystal VROS for $V_0 = 18$ Vrms at $f_0 = 200$ Hz, and $I_0 = 8.07$ mW/cm^2. (a) Experimental VROS observed through crossed linear polarizers. (b) Binarized and smoothed vertical interference fringe pattern of experimental measurements using positive helicity circular polarization. (c) Experimental estimation of geometric phase induced by LCLV using the Hilbert transform method. (i), (ii), and (iii) account for different VROS: single, triad, and quintet vortex, respectively.

By introducing the above ansatz into the director equation, linearizing in $\mathbf{W}$, and imposing a solvability condition after straightforward calculations, one obtains the dimensionless real Ginzburg–Landau type equation with topological forcing [25]:

$$\partial_\tau A = (\mu_0 + \mu_1 I(r))A - |A|^2 A + \nabla^2 A + \delta\partial_{\eta\eta}\bar{A} - f(r)e^{i\theta}, \quad \textbf{(2)}$$

where $A \equiv (X+iY)/\sqrt{\left[\pi^2(3K_3 - 2K_1) - 3\epsilon_a V_0^2\right]/4d^2}$ is the complex amplitude, $\mu_0 = -K_3(\pi/d)^2 - \epsilon_a V_0^2/d^2$ and $\mu_1 = 2\epsilon_a \alpha V_0/d^2$ are the homogeneous and spatial bifurcation parameters, respectively, $\delta \equiv (K_1 - K_2)/(K_1 + K_2)$ accounts for elastic anisotropy, $f(r) \equiv \epsilon_a 2dE_r(r)E_z(r)/z\pi \approx f_0 dI(r)/dr$ is the light forcing, and space and time are dimensionalized appropriately. A detailed derivation of Eq. (2) from first principles is presented in Ref. [25]. A similar amplitude equation with complex coefficients has been derived for a nonlinear optical cavity pumped by an orbital angular momentum beam [33]. Figure 4 shows the numerical simulations of Eq. (2) forced with a donut-shaped intensity $I(r) = Ar^2 e^{-r^2/2\omega^2}$.

Numerical simulations were performed using a triangular finite element code with adaptive spatial and temporal discretization, based on a second-order implicit backward differentiation method. The simulations were conducted within a computational domain of size 1001×1001. To compare these simulations with linear optical polarization microscopy, we defined the polarization field $\Psi = |Re\{A\}Im\{A\}|$ [see Fig. 4(b)]. For low intensities, the donut-shaped intensity profile induces a Rayleigh vortex with a singularity at its center, and its phase cut wraps around the ring [cf. Fig. 4(c(i))].

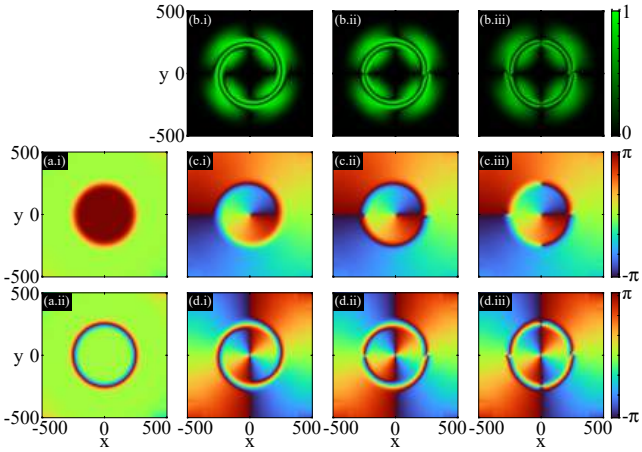

Fig. 4. Numerical simulations of the amplitude Eq. (2) for $\omega = 250$, $\mu_0 = -0.2$, $\delta = 0.4$, and $f_0 = 3\mu_1$. (a) Phase excess present in single vortex: (i) and (ii) are the phase in the complex field and the geometrical phase induced in light, respectively. (b), (c), and (d) are the polarization (Ψ) and phase of the complex field and the phase induced on the light, respectively. (i), (ii), and (iii) account for single ($\mu_1 = 0.15$), triplet ($\mu_1 = 0.2$), and quintet ($\mu_1 = 0.25$) of vortices, respectively.

For the Rayleigh vortex, we can separate the phase singularity from the total phase, observing a π phase excess in a region close to the position of the central phase singularity [see Fig. 4(a(i))]. This inhomogeneous phase excess in the liquid crystal system is transformed into an inhomogeneous geometric phase induced in the light, as seen in Fig. 4(a(ii)).

For large intensities, the solutions generate a triad vortex, composed of Rayleigh vortices encircled by a single pair of standard coupled vortex-antivortex. Figures 4(b(ii)), 4(c(ii)), and 4(d(ii)) show the polarization field, the phase in the liquid crystal system, and the geometric phase of the light, respectively. Increasing the forcing and using a larger number of vortices as the initial conditions reveals new equilibrium states among the vortices. For instance, in Figs. 4(b(iii)), 4(c(iii)), and 4(d(iii)), we identify a quintet of vortices and their respective phase in matter and light. Note that our numerical observations qualitatively align well with the configurations observed experimentally.

In summary, our experimental and theoretical results demonstrate that illuminating an optical valve with a vortex beam leads to the formation of optical vortex rosettes. These states feature a central Rayleigh vortex surrounded by multiple pairs of oppositely charged vortices in equilibrium. To elucidate the origin of these vortex rosettes, we derived an amplitude equation from first principles. Our findings suggest that light beams with donut-shaped profiles that could present topological properties, such as OAM beams, can create unexpected bound states of phase singularities in soft matter. These states, in turn, induce a nontrivial increase in topological defects and generate spatially inhomogeneous geometric phases, thereby opening a new pathway for optical vortex generation.

Funding. Agencia Nacional de Investigación y Desarrollo (ICN17_012); Fondo Nacional de Desarrollo Científico y Tecnológico (1250156); Centro de Modelamiento Matemático, Facultad de Ciencias Físicas y Matemáticas (FB210005); Hellenic Foundation for Research and Innovation (016097).

Acknowledgment. M.G.C and M.D.Z. is thankful for the financial support from ANID-Millenium Science Initiative Program-ICN17_ 012, Chile (MIRO). M.K. is thankful for the financial support from FONDECYT 1250156 and CMM ANID project FB210005. The research project of P.S. is implemented within the framework of H.F.R.I call "Basic research Financing (Horizontal support of all Sciences)" under the National Recovery and Resilience Plan "Greece 2.0" funded by the European Union – NextGenerationEU (H.F.R.I. Project Number: 016097).

Disclosures. The authors declare no conflicts of interest.

Data availability. Data underlying the results presented in this paper are not publicly available at this time but may be obtained from the authors upon reasonable request.

REFERENCES

1. A. S. Desyatnikov, Y. S. Kivshar, and L. Torner, *Progress in Optics*, E. Wolf, ed. (Elsevier, 2005), Vol. **47**, p. 291.
2. J. Wang, J.-Y. Yang, I. M. Fazal, *et al.*, Nat. Photonics **6**, 488 (2012).
3. A. E. Willner, K. Pang, H. Song, *et al.*, Appl. Phys. Rev. **8**, 041312 (2021).
4. F. Tamburini, G. Anzolin, G. Umbriaco, *et al.*, Phys. Rev. Lett. **97**, 163903 (2006).
5. M. Ritsch-Marte, Philos. Trans. R. Soc. A **375**, 20150437 (2017).
6. A. M. Yao and M. J. Padgett, Adv. Opt. Photonics **3**, 161 (2011).
7. H. H. Arnaut and G. A. Barbosa, Phys. Rev. Lett. **85**, 286 (2000).
8. A. Forbes, L. Mkhumbuza, and L. Feng, Nat. Rev. Phys. **6**, 352 (2024).
9. D. G. Grier, Nature **424**, 810 (2003).
10. V. G. Shvedov, A. V. Rode, Y. V. Izdebskaya, *et al.*, Phys. Rev. Lett. **105**, 118103 (2010).
11. M. Padgett and R. Bowman, Nat. Photonics **5**, 343 (2011).
12. L. Allen, M. W. Beijersbergen, R. J. C. Spreeuw, *et al.*, Phys. Rev. A **45**, 8185 (1992).
13. M. W. Beijersbergen, L. Allen, H. E. L. O. van der Veen, *et al.*, Opt. Commun. **96**, 123 (1993).
14. V. Y. Bazhenov, M. V. Vasnetsov, and M. S. Soskin, JETP Lett **52**, 429 (1990).
15. Z. Sacks, D. Rozas, and G. A. Swartzlander, J. Opt. Soc. Am. B **15**, 2226 (1998).
16. L. Marrucci, C. Manzo, and D. Paparo, Phys. Rev. Lett. **96**, 163905 (2006).
17. E. Brasselet, N. Murazawa, H. Misawa, *et al.*, Phys. Rev. Lett. **103**, 103903 (2009).
18. E. Brasselet, Phys. Rev. Lett. **108**, 087801 (2012).
19. E. Brasselet, Phys. Rev. Lett. **121**, 033901 (2018).
20. E. Calisto, M. G. Clerc, and V. Zambra, Phys. Rev. Res. **2**, 042026(R) (2020).
21. R. Barboza, U. Bortolozzo, G. Assanto, *et al.*, Phys. Rev. Lett. **109**, 143901 (2012).
22. R. Barboza, U. Bortolozzo, G. Assanto, *et al.*, Phys. Rev. Lett. **111**, 093902 (2013).
23. R. Barboza, U. Bortolozzo, M. G. Clerc, *et al.*, Adv. Opt. Photonics **7**, 635 (2015).
24. E. Calisto, M. G. Clerc, M. Kowalczyk, *et al.*, Opt. Lett. **44**, 2947 (2019).
25. P. J. Aguilera-Rojas, M. G. Clerc, M. Diaz-Zuniga, *et al.*, Phys. D **476**, 134599 (2025).
26. See Supplementary Material (Supplement 1) for videos.
27. I.-C. Khoo, *Liquid Crystals* (John Wiley Sons, 2022).
28. P. G. de Gennes and J. Prost, *The Physics of Liquid Crystals*, (Oxford Science Publications, Clarendon Press, 1993).
29. S. Chandrasekhar, *Liquid Crystals* (Cambridge University Press, 1992).
30. A. Gerrard and J. M. Burch, *Introduction to Matrix Methods in Optics* (Dover, 1975).
31. M. V. Berry, Proc. R. Soc. A **392**, 45 (1984).
32. S. Pancharatnam, Proc. Indian Acad. Sci. A **44**, 247 (1956).
33. S. Kumar, W. B. Cardoso, and B. A. Malomed, Symmetry **16**, 470 (2024).